One-class SVM based outlier detection strategy to detect thin interlayer debondings within pavement structures using Ground Penetrating Radar data

Shreedhar Savant Todkar, Vincent Baltazart, Amine Ihamouten, Xavier Dérobert, David Guilbert

Version of Record: https://www.sciencedirect.com/science/article/pii/S0926985121001397
Manuscript_0605a9221fe5f4602a12945bd2faa40b

One-class SVM based outlier detection strategy to detect thin interlayer debondings within pavement structures using Ground Penetrating Radar data

Shreedhar Savant Todkar[a,*], Vincent Baltazart[a], Amine Ihamouten[b], Xavier Dérobert[c], Cédric Le Bastard

[a] *Department of Components and Systems (COSYS - SII), University Gustave Eiffel, Nantes Campus, 44344 Bouguenais, France.*
[b] *Department of Materials and Structures (MAST - LAMES), University Gustave Eiffel, Nantes Campus, 44344 Bouguenais, France.*
[c] *Assessment and Imaging Laboratory (GERS - GeoEND), University Gustave Eiffel, Nantes Campus, 44344 Bouguenais, France.*

Abstract

In this paper, we present a processing method to detect millimeter interlayer debondings from Ground Penetrating Radar (GPR) B-scan images. The method is matched to carry out rapid debonding detection at the operational level. A machine learning based outlier-detection strategy namely, One-class Support Vector Machines (OCSVM) is proposed to detect A-scan data vectors which differ from a reference data set collected over a known healthy pavement area.

OCSVM is tested on both simulated and experimental data representing GPR data over various artificial millimetric debondings at $2.6\,\mathrm{GHz}$ and $4.2\,\mathrm{GHz}$ from respectively ground-coupled and air-coupled radar configurations. The experimental data were collected at the Accelerated Pavement Test site located in the Nantes campus of Université Gustave Eiffel. The simulated models on the other hand were generated using a numerical EM solver based on Finite Difference Time Domain (FDTD) method namely, GprMax. Simulation tests allow to conduct sensitivity analysis to determine the robustness of the detection method at various signal-to-noise ratios ($10\,\mathrm{dB}$ to $60\,\mathrm{dB}$).

The proposed OCSVM method demonstrated high performance on both simulated and experimental data to detect thin interlayer debondings over various GPR configurations.

Keywords: Ground Penetrating Radar (GPR), thin debondings, One-class SVM (OCSVM), Air-coupled radar, Ground-coupled radar, Sensitivity Analysis, Finite Difference Time Domain (FDTD), GprMax.

1. Introduction

In the context of pavement monitoring, an early stage defect detection is of great importance to maintain its durability, conduct Life Cycle Assessments (LCA) and avoid significant failures (Büyüköztürk and Yu, 2006; Hajj et al., 2010). However, with the

*Corresponding author
Email addresses: shreedhar.todkar@univ-eiffel.fr (Shreedhar Savant Todkar), vincent.baltazart@univ-eiffel.fr (Vincent Baltazart), amine.ihamouten@univ-eiffel.fr (Amine Ihamouten), xavier.derobert@univ-eiffel.fr (Xavier Dérobert), cedric.lebastard@gmail.com (Cédric Le Bastard)

passage of time and heavy traffic, extreme variations in weather conditions and water seepage, two types of pavement damages tend to occur: Surface and subsurface defects (Wright et al., 2014). In this paper, we focus on the latter type of defects, especially horizontal inter-layer cracks. The inter-layer cracks, called debondings (or delaminations), usually appear between the top two layers of the pavement (Todkar et al., 2017). These defects may give rise to stripping and/or reflexive cracks that lead to open surface cracks severely degrading the structural integrity of the pavement. Non-destructive testing (NDT) is one such technique that has been widely be used in this aspect.

Ground Penetrating Radar (GPR) is one well-known NDT electromagnetic method used in the field of Civil engineering for Non-destructive Testing (NDT) applications. (Wai-Lok Lai et al., 2018) provides an overview of the 30-year journey of GPR technology in civil engineering. Owing to its non-invasive capability and the sensitivity to material permittivity, GPR has been used in the literature for various applications including water content measurement (Kaplanvural et al., 2018), rebar corrosion in concrete (Zaki et al., 2018), pavement layer thickness estimation (Pinel et al., 2009), subsurface defects (Dong et al., 2016), anti-personnel mine detection (Ebrahim et al., 2018; Tellez and Scheers, 2017) *etc*.

In this paper, we focus on the detection of the horizontally stratified thin debondings that occur at the interface between the top two layers of the pavement structures. However as mentioned in (Benedetto et al., 2017), GPR data require suitable processing techniques that can interpret and help in the decision making process (such as classification, identification *etc.*). This has motivated the development of specific signal processing techniques to conduct early detection of thin debondings.

Support Vector Machines (SVM) are generally implemented as they pose low computational complexity, since they are based on support vectors (Tbarki et al., 2017b). In addition, the convexity of the optimal problem characterizes the unique solution obtained using SVM. Two-class SVM has been used in (Todkar et al., 2019, 2018, 2017) on GPR data to classify data vectors into defective (debonding) and non-debonding (healthy) A-scan classes.

Although the Two-class classification provided some impressive results in these cases, it lacked some key aspects. Firstly, it required *a priori* knowledge about the two data classes during the learning step, which, is not always available (Salem and Stolfo, 2012). Secondly, the imbalance in the two data (debonding and non-debonding) classes during the learning step results in a lower performance of the method. Two-class SVM also generally demands a larger learning dataset for best performance as shown in (Todkar et al., 2019).

An alternative strategy is proposed here to detect debondings within pavement structures using One-class SVM (OCSVM). A unique reference data class is used to identify outlier subsurface pavement conditions. In this context, the outlier is defined as the A-scan vectors that deviate from the reference data set collected over healthy pavement sections. The proposed strategy is expected to be better matched to both the short-term condition of field test and the limited prior knowledge which is available at the operational level. In the literature, OCSVM method has been used along with GPR to detect buried landmines (Tbarki et al., 2017b, 2018). Within this scope, the machine learning OCSVM (Schölkopf et al., 2001) is applied for detecting outlier radar data vectors (*i.e.* A-scans). OCSVM is advantageous as it performs faster training and testing (Salem

and Stolfo, 2012) due to its simplistic classification model. It also eliminates the need for labeled two-class information during learning stage (Senf et al., 2006). Besides, as mentioned in (Tbarki et al., 2017a), the outlier data (*i.e.*, debonding data in our application) are either not readily available or they very costly to acquire.

The versatility of the proposed approach is illustrated with the data created using the Finite-Difference Time Domain (FDTD) method simulating two radar configurations: air-coupled and ground-coupled GPR data collected over the same pavement structure embedded with artificial debondings. OCSVM is thereafter formulated using some local signal features to provide the required refined signal analysis of the time domain GPR signatures. The method demonstrated a quick and efficient defect detection and classification for both simulated and experimental data over ground-coupled and air-coupled radar configurations.

In this paper, we present the experimental and simulated GprMax datasets used to test the proposed detection OCSVM method, and describe its approach. The simulated data are modeled using Ground-Coupled-GPR (GC-GPR) and Air-coupled Stepped Frequency GPR (SF-GPR) configurations. Throughout, OCSVM parameters are extensively tested by Sensitivity Analysis using GprMax data, followed by demonstrating its performance on experimental data.

2. Datasets for method tests and validation

In this paper, two types of datasets are used to test the proposed detection method: a pavement model generated using GprMax, and experimental data collected at our university's Accelerated Pavement Test (APT) site. Both datasets are acquired/generated using the two configurations: ground-coupled and air-launched GPR. We now present these two data sets.

2.1. Experimental datasets

To validate the OCSVM method over experimental data, the data is collected at IFSTTAR's* APT site (Simonin et al., 2012) (currently known as University Gustave Eiffel).

2.1.1. The Fatigue Carousel

The fatigue carousel situated at the Nantes campus of University Gustave Eiffel is a $120\,\mathrm{m}$ long and $6\,\mathrm{m}$ wide one off-circular outdoor APT test track. It facilitates several loading stages ($65\,\mathrm{kN}$ on single wheel, twin wheel, tandem or tridem axles) with various configurations and rotational speeds of up to $100\,\mathrm{km\,h^{-1}}$ which reproduces the effect of in-use traffic at an accelerated rate.

Of its $120\,\mathrm{m}$ test track, the site dedicates a $25\,\mathrm{m}$ section for our experiments. Here, a two-layered structure with the top layer (course layer) of about $5\,\mathrm{cm}$ to $6\,\mathrm{cm}$ thickness and the base layer of about $8\,\mathrm{cm}$ thickness over a granular sub-base are laid.

Three artificial rectangular defects of various thickness and material compositions are

*French Institute of Science and Technology for Transport, Development and Networks

embedded in this section (ref. Figure 1a). These defects namely, Geotextile, Sand and Tack-free based defects are monitored over several loading stages of 10K, 50K and 100K (where K indicates one thousand loading cycles/rotations of the fatigue carousel (Dérobert and Baltazart, 2012)). Geotextile and Sand based defects are defects with larger thicknesses presenting the highly degraded pavement conditions. Tack-free defects represent the lack of coating conditions between the pavement layers and as such, they closely resemble a realistic defective pavement structure with thin debondings. Thus, in this paper we present the debonding detection for the weakest defect type, namely, Tack-free. A coring test at the end of the pavement life-cycle showed that the maximum debonding thickness of Tack-free defect zone was within the range of $2\,\mathrm{mm}$ to $3\,\mathrm{mm}$. Figure 1a shows the embedded defects before laying the course layer. The zone I13 represents the Tack-free based defects (Simonin et al., 2016, 2012). For our experiments, this zone is used for data acquisition. The areas marked 'Zone I11' and 'Zone I12' respectively represent Geotextile and Sand-based defects which are not included in this paper. (Dérobert et al., 2020) provides the recorded data for both radar types and the detailed description of the test track with the three embedded defects.

The GPR probing pavement section consists of three layers (see Figure 1c): Layers 1 and 2 are asphalt surface pavements (with $\varepsilon_{r1} < \varepsilon_{r2}$) and Layer 3 represents the artificial debonding layer whose thickness ranges from $2\,\mathrm{mm}$ to $3\,\mathrm{mm}$ with $\varepsilon_{r1} < \varepsilon_{r2} < \varepsilon_{r,deb}$ for Tack-free defects. It should be noted that the permittivities may be reinforced by water seeping with time (Todkar et al., 2019).

2.1.2. Data collection

The data collection is done using the two main radar configurations which are used at the operational level. The first configuration is a ground-coupled commercial GPR namely, GSSI SIR-3000 (GSSI-GPR) operating at a peak magnitude centered at $f_c = 2.6\,\mathrm{GHz}$ in free space.

The GSSI-GPR uses a high-frequency quasi-monostatic transmitter-receiver (Tx - Rx) bow-tie antenna setup (Todkar et al., 2017). The radar allows data collection at traffic speed of up to $10\,\mathrm{km\,h^{-1}}$. The radar is capable to acquire up to 8192 samples per A-scan. However during experiments, a preset value of 1024 samples per A-scan is chosen with a time window duration of $8\,\mathrm{ns}$ and the data is collected at average walking speed. The GSSI-GPR uses a very small Tx - Rx offset maintaining it in a quasi-mono static configuration. Figure 2a shows the GSSI-GPR data acquisition setup at IFSTTAR's APT site.

The second GPR is an experimental air-coupled Step-frequency radar (SFR) whose peak magnitude is centered at $f_c = 4.2\,\mathrm{GHz}$ in free space with frequency bandwidth BW = $0.8\,\mathrm{GHz}$ to $10.8\,\mathrm{GHz}$. The SFR uses an ultra-wideband exponentially tapered slot antennas (Diakité et al., 2015) and collects the data in frequency domain at limited speed thanks to a Vector Network Analyzer (VNA). The frequency data is converted to time domain data using inverse Fourier transform for processing by OCSVM. The SFR time range is limited to $6\,\mathrm{ns}$ and includes 5000 samples per A-scan. The SFR, has an offset of $0.2\,\mathrm{m}$ between the Tx and Rx and is thereby in a bi-static configuration. Figure 2b shows the SFR data acquisition setup.

Thanks to toolbox provided by (Nesbitt et al., 2019), the GSSI data is easily accessed for processing on the Python environment. On the other hand, an inverse Fourier trans-

(a) 25 m track with artificial defects before laying the wearing course layer. 'Zone I13' indicates Tack-free based defects (Zones I11 and I12 are respectively Geotextile and Sand-based defects)

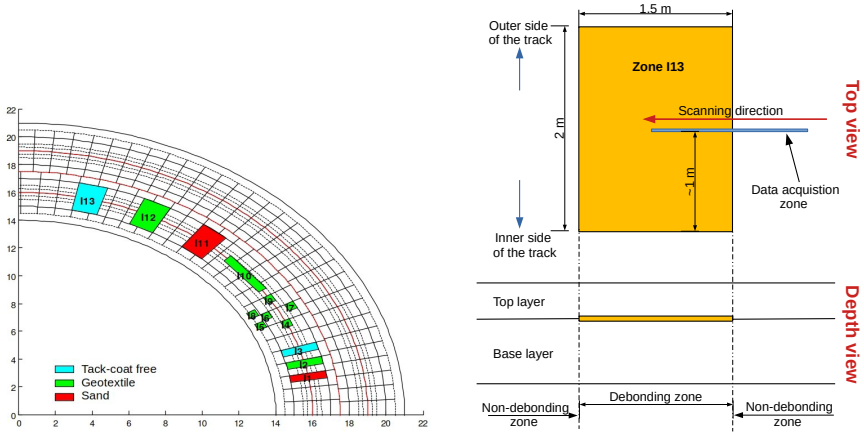

(b) Location of each embedded defect sections. Zone 'I13'represents the Tack-free defects that was used for data acquisition (Dérobert et al., 2020)

(c) Top and Lateral views of the test section (Zone I13 or Tack-free)

Figure 1: APT Test track at Univ. Gustave Eiffel

form is used on the SF-GPR data for processing.

2.2. *Numerical modeling using GprMax*

For preliminary validation of the debonding detection method, we use an FDTD-based method that is used to generate subsurface models using EM wave propagation namely GprMax (Warren et al., 2015). Since we perform a 2D analysis, a 2D pavement model of dimensions $3.0\,\mathrm{m} \times 0.28\,\mathrm{m}$ is created. The domain size of the model is set to $3.0\,\mathrm{m} \times 1.0\,\mathrm{m}$. The spatial and temporal discretization sizes (or mesh size) used are respectively $\Delta x = 1 \times 10^{-3}\,\mathrm{m}$ and $\Delta y = 5 \times 10^{-4}\,\mathrm{m}$. The temporal resolution is set to $\Delta t = 1.45 \times 10^{-12}\,\mathrm{s}$ such that the stability condition known as CFL (Courant, Freidrichs, Lewy) condition is satisfied (Giannopoulos, 2005). The point source is a Hertzian dipole polarized in z-axis.

The pavement model used with GprMax is as shown in Figure 3. The model consists

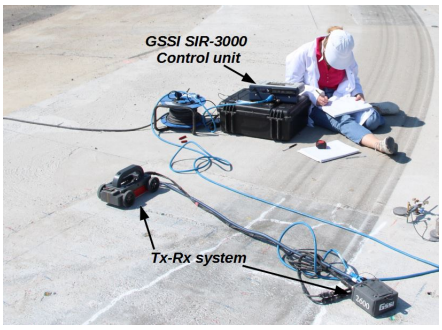

(a) GSSI GPR setup

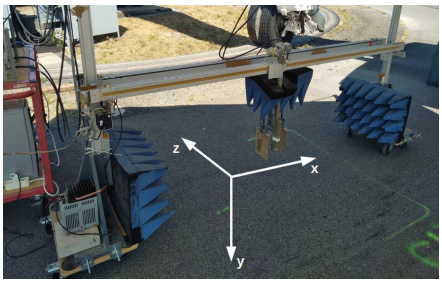

(b) Step-frequency GPR setup (Dérobert et al., 2020). The 'x'-axis (or spatial axis) represents the scanning direction, 'y'-axis (or time axis) is the depth and 'z'-axis is the lateral axis

Figure 2: Data acquisition setup at IFSTTAR's APT site

of two or three layers depending on the zone, which is divided into Non-debonding zone (two layers) and Debonding zone (three layers). The top course layer has relative permittivity of $\varepsilon_{r1} = 5$ and of thickness $0.08\,\mathrm{m}$. The base layer on the other hand has permittivity of $\varepsilon_{r2} = 7$ with thickness $0.2\,\mathrm{m}$.

In reality, an interlayer debonding may be composed of (a) air voids or water/moisture voids, (b) mixture of the pavement material from adjacent layers, or, (c) a combination of all of the above. In this paper, we focus on the detection of air-void defects. The debonding layer thus has a relative permittivity of $\varepsilon_{r,deb} = 2$ (value is used to incorporate '*near air-void*' defects) and the debonding thickness is assigned as $th_{deb} = 3\,\mathrm{mm}$ (other values for th_{deb} have been also studied in the later sections).

In addition, it should be noted that whilst creating the model, the following assumptions were made:

1. Pavement layers are assumed to be homogeneous
2. Smooth surfaces and interfaces
3. Top layer is sufficiently thick to avoid overlapping of surface and interface echoes
4. Debonding thickness is smaller than the quarter of the wavelength (*i.e*, $th_{deb} \leq \lambda_{deb}/4$, where λ_{deb} is the wavelength within the debonding layer)

The excitation waveform in the case of ground-coupled GPR is a Gaussian centered at $f_c = 2.6\,\mathrm{GHz}$ whose antennas are positioned in contact with the surface (*i.e*, $h_{ant} =$

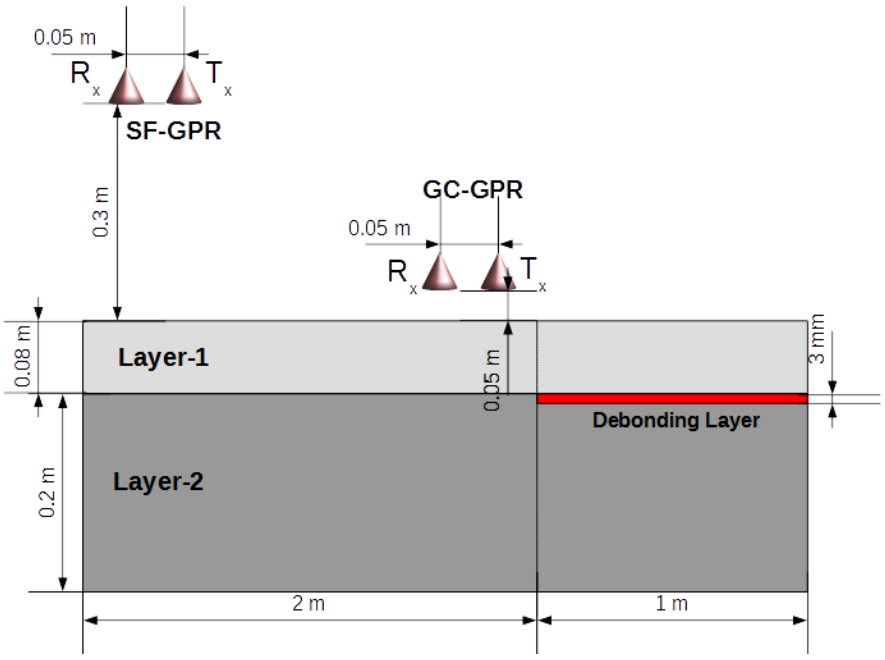

Figure 3: Generated pavement model using gprMax

$0.05\,\mathrm{m}$). These parameters are set to imitate the GSSI-GPR used in the experimental data (see Section 2.1). The distance between Tx and Rx is set to $0.05\,\mathrm{m}$. For the air-launched GPR, the excitation waveform is the first Gaussian derivative centered at $f_c = 4.2\,\mathrm{GHz}$ with $h_{ant} = 0.3\,\mathrm{m}$ and the distance between Tx and Rx being $0.05\,\mathrm{m}$. In both cases, the adjacent A-scans possess a spatial separation of $0.01\,\mathrm{m}$. On the pavement model, the acquisition avoids the PML (Perfectly Matched Layer) zone of the model. In addition, 25 A-scans on both sides of the pavement model are ignored to eliminate the A-scans with edge effects.

A total of 150 A-scans are acquired to create a B-scan consisting on 50 A-scans for debonding case and 100 A-scans for non-debonding case. The B-scans are generated to approximate the two radar configurations used in the experiments.

3. OCSVM for Thin debonding detection

In this section, we present the different preprocessing techniques and the detection process based on the proposed method for rapid short-term debonding detection. Short-term detection refers to the debonding detection spanning over various time intervals carried out without prior knowledge of the initial conditions of the pavement. This approach enables the operator to efficiently locate debondings (outliers) even from large GPR datasets.

3.1. Basics on GPR time signatures

For our application, the top two pavement layers are studied. As mentioned in (Todkar et al., 2019), in case of a healthy pavement, two reflected echoes are obtained: backscattered echo from the top surface of the pavement and echo from the interface between the first and the second pavement layers. The signal amplitude is proportional to the contrast in the dielectric of the two media (pavement layers).
In case of a debonded pavement, three echoes are expected. The first is the backscattered surface echo while the two subsequent echoes are reflections from the upper and the lower interfaces of the debonded layer that overlap in time domain. This overlapping is mostly constructive as long as the debonding thickness is limited by the quarter wavelength ($th_{deb} \leq \lambda_{deb}/4$) (Todkar et al., 2019). Since the amplitude of the reflected echo depends on the dielectric contrast at each interface of the stratified medium, the first (or surface) echo is the strongest whereas the second strongest echo is seen at the interface (healthy and debonded zones) and can be up to $\frac{1}{10}$th of the surface echo. Then, the peak magnitude of the second strongest echo is used to center the time window. Therefore, the echoes can be identified based on both the amplitude and time delays.

3.2. Pre-processing GPR data

Signal features can be generally defined as the characteristics of a data set that contains sufficient information to distinguish among the classes of data (Liu and Motoda, 1998; Siegwart et al., 2011), which, in our application are debonding and non-debonding classes.
The useful information expected from the signal features are that they (a) retain the characteristics of the original data (b) are limited in number, and, (c) are unaffected by unwanted variability in the input data (Kumar and Bhatia, 2014). The study of the use of signal features in this paper is necessary as it helps to:

- validate the adaptability of OCSVM for various input data types (*i.e.*, Sensitivity Analysis)
- reduce the processing data size and complexity
- avoid over-learning/over-fitting that may hinder the performance, and,
- possibly improve the debonding detection rate

Signal features can either be global or local depending on the zone from where they are extracted. (Peeters, 2004) defines global features as the characteristics computed from the complete signal and local features as the characteristics computed within a specific time window.
For our application, we define the global and local features by the size of the time-gating window. The global features are computed within the time window that encompasses the surface and the interface echo, which, as shown in Figure 4 for experimental data is approximately between $1.84\,\mathrm{ns}$ and $4.7\,\mathrm{ns}$. The time-gating window to compute local features on the other hand, is limited at the interface (*i.e.*, echo between the top

and base pavement layers). The length of time gating window (W_{tg}), in terms of number of samples for local features is a function of the center frequency of the GPR pulse given by (Todkar et al., 2019):

$$W_{tg} = 2 \times \{f_s \times t_w\} \tag{1}$$

where, f_s is the sampling frequency and t_w is the pulse width of the emitted GPR pulse.

A tapered Tukey-cosine window is used for the interval W_{tg} in order to extract local

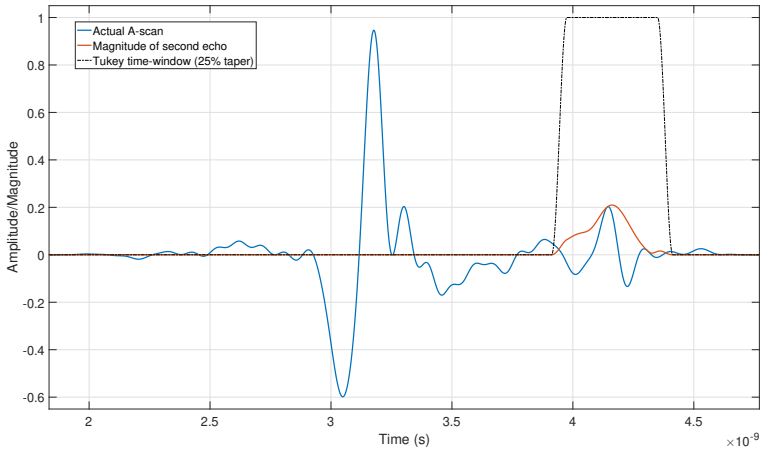

Figure 4: Time-gating window for an A-scan from APT data (Tack-free based defects at 10K loading) (Todkar, 2019)

features. For better representation, Figure 4 shows an A-scan with the window. Figure 5 compares a B-scan before and after the time gating is performed.

Following (Todkar et al., 2019), the local signal features are used in this paper to achieve better debonding detection.

For the sake of comparison, this paper uses the same local signal features listed in Table I of (Todkar et al., 2019). This local feature set consists of 10 signal features for each A-scan data vector. These features are chosen using the Ground truth (GT) associated to a known GPR dataset to perform the feature selection. GT categorizes the A-scans into two classes, namely debonding and non-debonding cases. The probability density function (PDF) of the features is computed over each class to determine those which are sensitive enough to the pavement conditions. The separation between the two curves is used to choose the best features for our application (Todkar et al., 2019). In order to use the OCSVM method, the feature matrix ($\mathbf{F}_{mat}$) is column-normalized (A-scan by A-scan) between [-1, 1] using Min-Max normalization. By normalization, the impact of large valued features extracted on a different scale is reduced allowing small valued features to contribute equally.

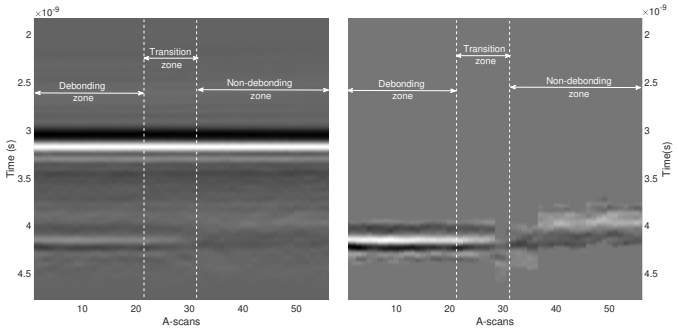

Figure 5: Comparison of the original and the time-gated B-scans from APT data (Tack-free based defects at 10K loading) (Todkar, 2019). The amplitudes in both images have been normalized for visualization

3.3. Proposed debonding detection method

(Schölkopf et al., 2001) introduced the OCSVM as a method of adapting SVM to a one-class classification problem.

For OCSVM, the learning data consists only in non-debonding data and the origin is the only member of the debonding data set (by contrast, SVM would require the learning data set to include both debonding and non-debonding data). Figure 6 shows the geometrical interpretation of OCSVM.

OCSVM can be obtained using Support Vector Data Description (SVDD) wherein the

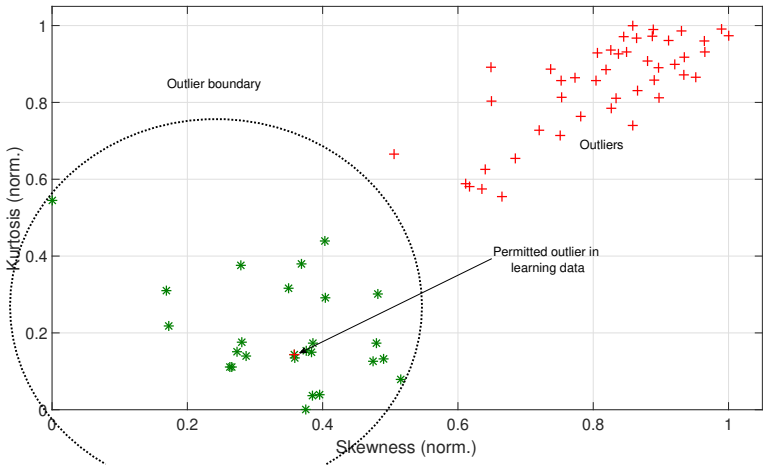

Figure 6: Geometrical representation of a OCSVM using two signal features (kurtosis and skewness) from APT data (Sand-based defects)

data-points are mapped onto a higher dimension circumscribed by a hyper-sphere (Tax and Duin, 2004). This hyper-sphere acts as the limiting factor and the aim would be to

find this hyper-sphere with minimum radius that encompasses the positive (*i.e.* Non-debonding) data mapped on the said hyper-space.
To begin with, we first define a closed hyper-sphere around the known non-debonding learning feature set in the hyper-space. This sphere is defined by its radius $R > 0$ and centered at b. The learning set strictly contains the data-vectors of only one type of data and is given by: $\mathbf{X}_{mat} = \mathbf{x}_1, \mathbf{x}_2 \ldots, \mathbf{x}_N$ where N is the number of learning data-vectors and $\mathbf{X}_{mat} \in \mathbf{F}_{mat}$ is the feature matrix of the known non-debonding zone.
We aim to minimize the volume of this hyper-sphere by minimizing the radius R keeping in mind that all the learning points are embedded within this hyper-sphere. To do so, as (Tax and Duin, 2004) mentions, an error function is defined analogous to Support vector classifiers as:

$$\begin{aligned} & f(R, b) = R^2 \\ & \text{constrained to: } ||\mathbf{x}_i - b||^2 \leq R^2 \; \forall \; i \end{aligned} \tag{2}$$

Now, to allow all possibilities of the outliers into the learning set, the distance between each data-vector $\mathbf{x}_i$ and the center of the hyper-sphere b should be less than R^2. If this condition is not satisfied, the distances larger than this should be penalized. To do so, a positive slack variable ξ_i (where $\xi_i \geq 0$) is introduced. The minimization problem thus becomes (Chen et al., 2001; Tax and Duin, 2004):

$$\begin{aligned} & minimize_{R,\xi,b} \; f(R, b, \xi) \; = R^2 + \frac{1}{\nu N} \sum_{i=1}^{N} \xi_i \\ & \text{s.t.} \quad ||\mathbf{x}_i - b||^2 \leq R^2 + \xi_i, \; \forall i = 1, 2, \ldots N \end{aligned} \tag{3}$$

where,

- ν is a user designed parameter that is used to determine the amount of admitted slack (*i.e.* amount of outliers permitted in the learning data)
- ξ_i is the introduced slack variable

Equation 3 is the standard form of convex quadratic programming problem which can be solved by introducing Lagrangian multipliers, α_i and β_i (Gu et al., 2010; Tax and Duin, 2004):

$$\mathcal{L}(R, b, \alpha, \beta, \xi) = R^2 + \frac{1}{\nu N} \sum_{i=1}^{N} \xi_i + \sum_{i=1}^{N} \alpha_i \Big[R^2 + \xi_i - ||\mathbf{x}_i - b||^2 \Big] + \sum_{i=1}^{N} \beta_i \xi_i \tag{4}$$

By solving the Lagrangian and substituting values, we obtain:

$$\mathcal{L}(R, b, \alpha, \beta, \xi) = \sum_{i} \alpha_i . \langle \mathbf{x_i}, \mathbf{x_i} \rangle - \sum_{i} \sum_{j} \alpha_i \alpha_j \langle \mathbf{x_i}, \mathbf{x_j} \rangle \tag{5}$$

The $\langle \cdot, \cdot \rangle$ dot product can be replaced with a kernel function ($\Phi(\cdot)$) in One-class SVM (Gu et al., 2010).
For cases where the data is linearly separable, $\Phi(\cdot)$ is a linear kernel, otherwise, a non-linear kernel (namely, Gaussian radial basis function, sigmoid or polynomial kernel (Chang and Lin, 2011)) is used. The boundary condition is then defined by R as:

$$||\Phi(\mathbf{x}_i) - b||^2 = R^2 \tag{6}$$

where,

- $\mathbf{x}_i$ is any support vector with $0 < \alpha_i < \frac{1}{\nu N}$
- α_i is the Lagrange multiplier

The OCSVM decision function $D(\mathbf{x})$ is given as:

$$D(\mathbf{x}) = sgn\{\Phi(\mathbf{x}_i) - b\} = \begin{cases} +1, & \text{for } f(x) \\ -1, & \text{for } \bar{f}(x) \end{cases}$$

where, $f(x)$ and $\bar{f}(x)$ are respectively inlier and outlier data predicted by OCSVM.

3.4. OCSVM programming

The anomaly debonding detection is implemented in Python Scikit-learn (Pedregosa et al., 2011) using the LIBSVM (Chang and Lin, 2011) library to create a outlier detection model. The latter model requires to select the kernel function in Equation 3 and its associated parameters according to the processing presented in the next section. The selected model is then used to identify the presence or absence of debondings (outliers) over the unknown pavement area.

The learning data size for synthetic GprMax and experimental data are respectively 30 and 20 adjacent A-scans from the healthy pavement zone. In case of simulated dataset, the learning data is considered separately for each individual noise level and debonding thickness. For experimental data, the learning data for each B-scan is acquired from the healthy pavement zone at their respective loading cycle of the fatigue carousel.

The outlier-detection model is generated using the learning data. A k-fold Cross validation technique (with $k = 3$) is used alongside a loss function to determine the model parameters. These parameters are then used to identify the presence or absence of debondings over the unknown test pavement area. Figure 7 briefly depicts the overall steps carried out to detect thin debondings using OCSVM.

Since learning data consists of only one type of data, it is expected to demonstrate similar performance levels at various values of learning data set size *i.e*, N_{learn}. Nevertheless, this analysis will be studied in the next section (Section 4.2.2).

3.5. Choice of OCSVM parameters

The selection of the kernel function and the associated parameters is conducted by optimizing the classification results over the training data set. In this paper, two kernel functions namely, linear and non-linear (Gaussian) have been compared on this basis. These kernel functions can be expressed as (Eude and Chang, 2018):

$$\Phi_{lin}(\mathbf{x_i}, \mathbf{x_j}) = \mathbf{x_i}^T \mathbf{x_j} + C \tag{7}$$

$$\Phi_{rbf}(\mathbf{x_i}, \mathbf{x_j}) = exp\{-\gamma ||\mathbf{x_i} - \mathbf{x_j}||^2\} \tag{8}$$

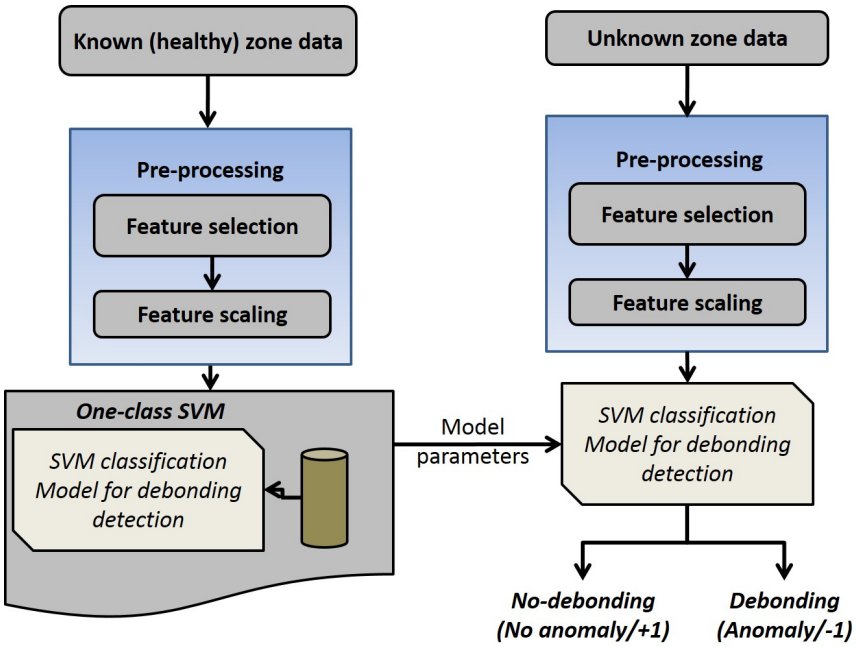

Figure 7: Debonding detection process (Todkar, 2019)

The linear kernel requires the optimization of a single parameter, namely, ν; whereas the Gaussian kernel uses both ν and γ parameters.

The Hinge loss is usually the preferred loss function since it is better suited for classification problems; by contrast, the root-mean square error would be preferred instead for regression problems (Todkar, 2019). For our intended output, the Hinge loss function only takes two discrete values [0, 2], *i.e.* non-zero values for misclassified A-scans (False Positive - FP and False Negative - FN values) and to zero values for properly classified A-scans (True Positive - TP value).

In order to gain further sensitivity in the optimization problem, the average Hinge-loss function is computed at each signal-to-noise ratios (SNR) over the 100 independent noise realizations, accordingly to the Monte-Carlo process. As a result, the average hinge loss function then takes intermediate step-wise value within the [0, 2] interval, as traced in both Figure 8 and Figure 9.

The search for the minimum hinge loss value is usually performed over a fine grid search in ν and γ. The user designed slack is limited to $\nu \in]0, 1]$. In practice, the ν-parameter decides the fraction of outliers present in the training data set (Mei and Zhu, 2015). Since the training dataset for simulated data is devoid of outliers, the value of ν is fixed to a low value, *i.e.*, $\nu = 0.001$. The optimum value is then expected to be small. On the other hand, the γ-parameter range is chosen from (Pedregosa et al., 2011), where the suitably sufficient range for γ is $[10^{-3}, 10^{3}]$.

Figure 8 presents the average hinge loss for the Gaussian kernel after 100 Monte-Carlo realizations at $30\,\mathrm{dB}$ SNR with 20 learning samples. As mentioned in the previous

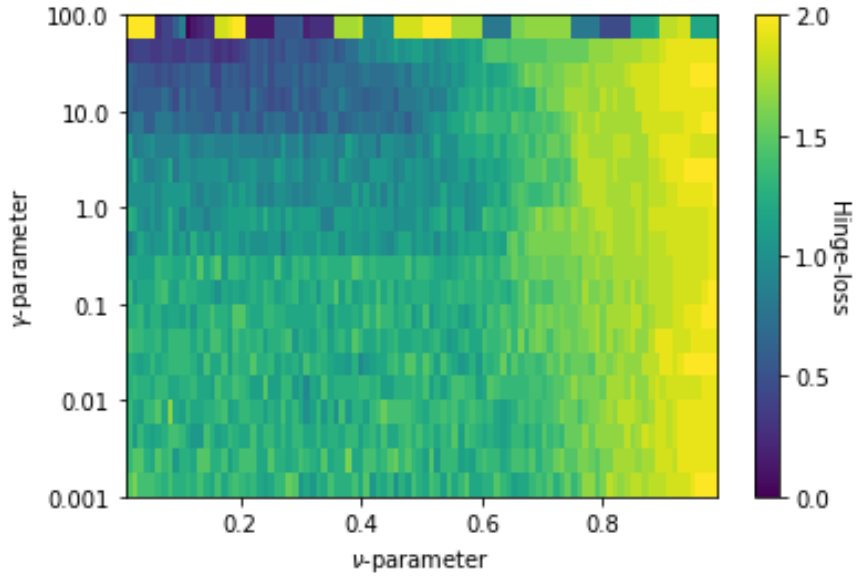

Figure 8: Variation of Hinge-loss function with respect to ν and γ parameters for a simulated gprMax B-scan image with SNR = 30 dB using 20 learning samples and th_{deb} = 3 mm

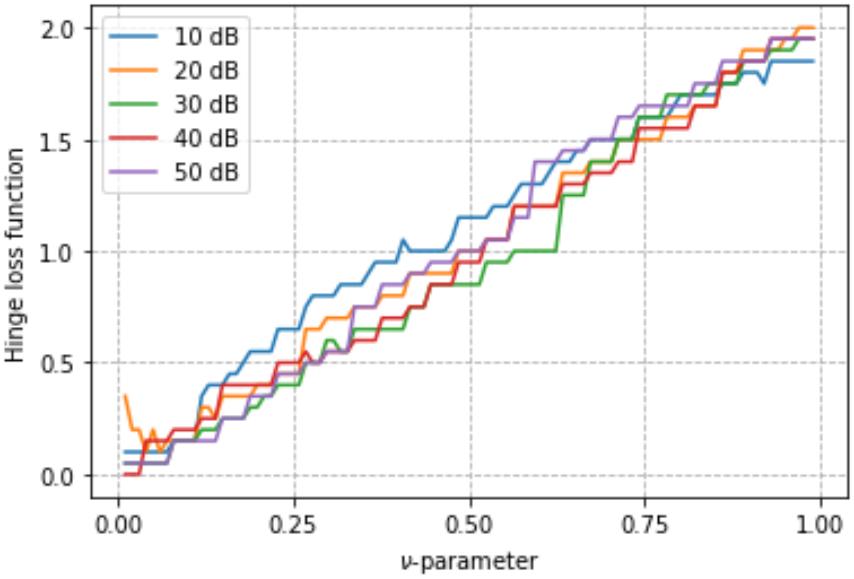

Figure 9: Variation of Hinge-loss function with respect to ν-parameter for a simulated gprMax B-scan image at various SNR levels using 20 learning samples and th_{deb} = 3 mm

section, a 3-fold cross validation is used here. It was observed that the function to minimize shows smooth step-wise variations with a global minimum loss function value observed at smaller ν and intermediate γ values. It is also shown that γ parameter has a small influence on the loss function at medium to high SNR levels. Further simulations have shown that, at lower SNR values, the Hinge-loss variations depends on both kernel parameters at once again smaller ν values and intermediate and/or high γ values. Due to the small influence on gamma-parameter, the linear kernel function has been preferred as kernel function for data with SNR = $30\,\mathrm{dB}$ or above, thereby reducing the computation to simply one parameter, namely, ν. Figure 9 shows the influence of ν over Hinge-loss values at various SNR levels. It can be confirmed that the optimum ν value is close to 0.001 and slightly depends on SNR. By contrast, the Gaussian kernel would be better suited for data of SNR = $20\,\mathrm{dB}$ or below.

3.6. Metrics to assess OCSVM performance

A benchmark, called as Ground Truth (GT) is established for each dataset. GT refers to the accurate interpretation and labeling of the pavement conditions under controlled tests. While the GT is used for the synthetic GprMax data, the experimental data uses the Pseudo Ground Truth (PGT), which is a roughly estimated benchmark of pavement conditions. In both cases, the debonding A-scan is assigned to 1 and the non-debonding A-scan is assigned to -1.
The OCSVM detection can result in one-out-of-four possible outcomes namely: True Positive (TP), False Positive (FP), True Negative (TN) and False Negative (FN). These four values are collectively grouped as a Confusion Matrix (Kulkarni et al., 2020). This matrix is used to compute the Dice score (DSC) that describes the performance of OCSVM model.
Furthermore, for the sake of reliability, the transition zone between debonding and healthy zones is not included in the performance assessment for both simulated and experimental data.

4. Tests and validation of GprMax model

In this section we analyze the performance of the detection method on pavement model generated using GprMax.

4.1. Noiseless simulated data

Figure 10a and Figure 10b illustrate the detection results of the OCSVM method for the two radar technologies. The classification labels in the figures use -1 to indicated Non-debonding and +1 for debonding labels.
Due to the absence amount of variation in the feature distribution for the healthy zone (non-debonding A-scans along the scanning direction), a small data size ($N_{learn} = 20$) is sufficient for the learning step. Due to the ideal smooth interface B-scan data, it was observed that OCSVM presented an excellent detection result with zero false detection. As mentioned in Section 3.5, a linear kernel was used and the value for ν parameter was set to 0.001.
However, in order to explore the OCSVM capability to adapt to various pavement configurations and scenarios, Sensitivity analysis is presented hereafter.

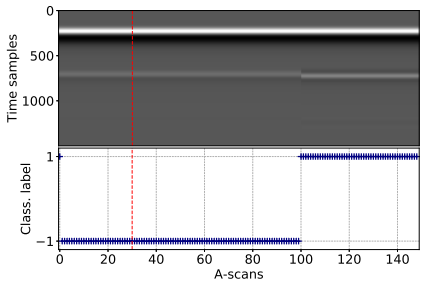

(a) Ground coupled GPR configuration

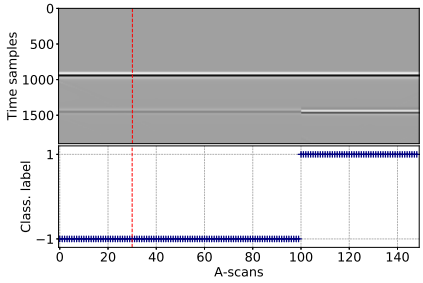

(b) Air-launched GPR configuration

Figure 10: OCSVM debonding detection on noiseless GprMax data with debonding thickness th_{deb} = $3\,\mathrm{mm}$. The vertical dashed line indicates the learning data

4.2. Sensitivity Analysis

Sensitivity analysis (SA) is the study of uncertainties between a given input and its expected output (Samadzadegan et al., 2010). Using SA, we can also determine the robustness and adaptability of OCSVM over various GPR technologies and pavement configurations. In this section, we present the OCSVM-SA with respect to, noise level and learning data size.

4.2.1. Effect of Noise

Noise plays an important role in the consistency of the signal and as such, the noise level in the signal sometimes limits the performance of the detection methods. The noise level is decided by the standard deviation of the noise given by:

$$\sigma_N = \frac{M}{10^{(\frac{SNR}{20})}} \tag{9}$$

where,

- M is the maximum magnitude of the second echo of the signal (A-scan),
- σ_N is the standard deviation of the noise added,
- SNR is the signal-to-noise ratio in dB.

Using Equation 9, an ideal-White Gaussian noise is added to each B-scan image such that the noise samples are decorrelated to each other in both vertical (*i.e.*, time) and

horizontal (*i.e.*, between A-scans); the SNR has been varied between $10\,\mathrm{dB}$ to $60\,\mathrm{dB}$. The detection results presented are averaged over 100 independent noise realizations for each Ground-coupled and Air-launched GPR configurations.

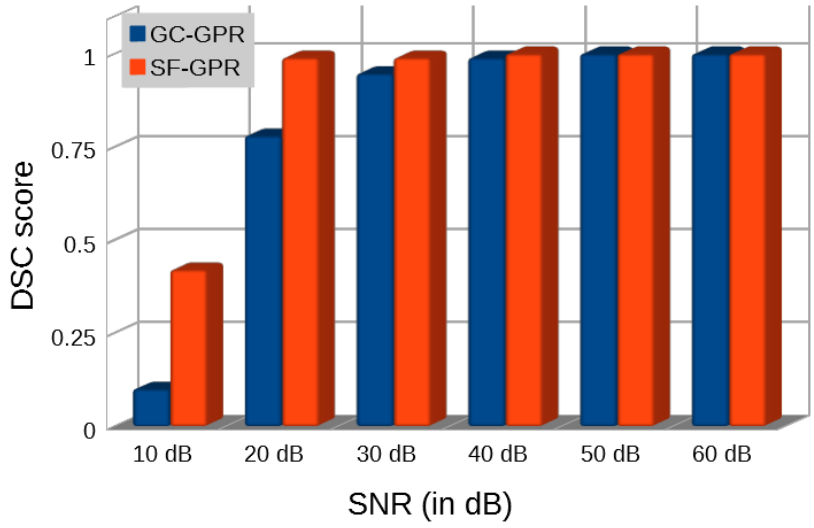

Figure 11: Comparison of average DSC score for GC-GPR and SF-GPR GprMax configurations at various levels of SNR for 100 independent Monte-Carlo realizations (th_{deb} = 3 mm, $N_{learn} = 30$)

Figure 11 traces the DSC score with respect to SNR for both GC-GPR and SF-GPR configurations. For the two GPR configurations, it is observed that at SNR = $10\,\mathrm{dB}$, the debonding detection indulges a high false-detection rate (both FP and FN) leading to reduced performance.

However, the performance rapidly improves above 0.75 beyond SNR = $20\,\mathrm{dB}$. In all cases, the detection rate is higher for SF-GPR data compared to GC-GPR. The higher frequency and larger frequency bandwidth provide better time resolution to SFR radar, that provides better separation of surface and interface echoes. This conclusion is worth over all levels of SNR according to Figure 11, but also for any thickness as well according to (Todkar, 2019).

During this analysis, the learning data size was chosen by intuition. However, the learning data has an effect over the performance of SVM as stated in (Huang, 2001; Thomas et al., 2015). Thus, in the following section, the sensitivity of the OCSVM is tested with respect to, the learning data size and its effect on the debonding detection rate.

4.2.2. Effect of learning data size

For Two class SVM, learning to test data ratio used in the literature varies from as low as $\frac{1}{5}$th (Huang, 2001) to as high as $\frac{4}{5}$th (Thomas et al., 2015).

On the other hand, in case of OCSVM, the literature suggests to use $\frac{2}{3}$rd of the data for

learning (Dreiseitl et al., 2010; Li et al., 2003). Since One-class SVM relies on only one type of data to create the classification model, the dependability of the learning data size is inclined on the variations of the non-debonding data.

As specified in Section 4.1, the noiseless data presents no variation in the feature distribution. Thus the learning data size can be very small. However for noisy data, the learning data size is expected to play a vital role in the debonding detection. Therefore, in this section, we analyze the effect of learning data size on the performance.

Here, the debonding thickness is set to 3 mm and noise is added to obtain an SNR of 30 dB. Figure 12 traces the DSC score variation at increasing learning data sizes for both GC-GPR and SF-GPR configurations. These are obtained by a Monte-Carlo process averaged over 100 independent realizations for the two configurations.

It can be observed that, for both GC-GPR and SF-GPR configurations, for small learning datasets (= 5 A-scans), the debonding detection rate (DSC) is greater than 0.8. However a rapid increase in the performance (*i.e*, DSC) is observed up to $N_{learn} =$ 20 beyond which a gradual increase in DSC up to 1 was observed. This SA infers that the OCSVM method can be implemented on GPR datasets for debonding detection irrespective of its configuration.

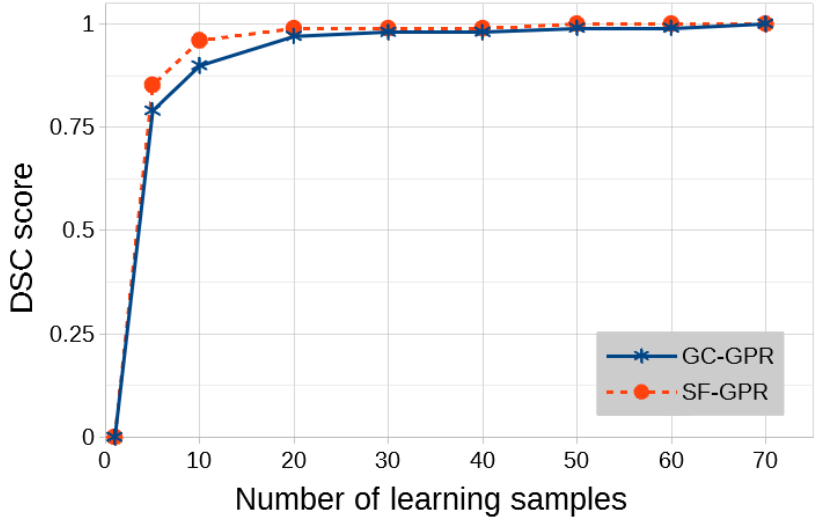

Figure 12: DSC variation with respect to learning data size for noisy GprMax data with SNR = 30 dB for ground-coupled and air-launched configurations (th_{deb} = 3 mm, $N_{learn} = 30$)

4.2.3. Effect of debonding thickness

In the previous sections, we studied the effect of various parameters such as noise, learning data size *etc*. on the performance. However, in every case, the debonding layer within the B-scan was fixed to one thickness (*i.e*, 3 mm). In this section, we analyze the performance behavior in conditions with different debonding thicknesses.

As done in previous sections, the detection is averaged over 100 independent Monte-Carlo realizations.

A B-scan is generated with the pavement parameters specified in Section 2.2. The defective zone consists of four sub-zones containing debondings of respectively $1\,\mathrm{mm}$, $3\,\mathrm{mm}$, $5\,\mathrm{mm}$ and $7\,\mathrm{mm}$ thicknesses (as depicted in Figure 13). Each defective zone is $0.2\,\mathrm{m}$ long with 20 acquired A-scans whereas the non-defective zone is $1\,\mathrm{m}$ long with 100 acquired A-scans. Thus, the resulting B-scan contains a total of 180 A-scans.

Figure 14a and Figure 14b respectively present the debonding detection for GC-GPR

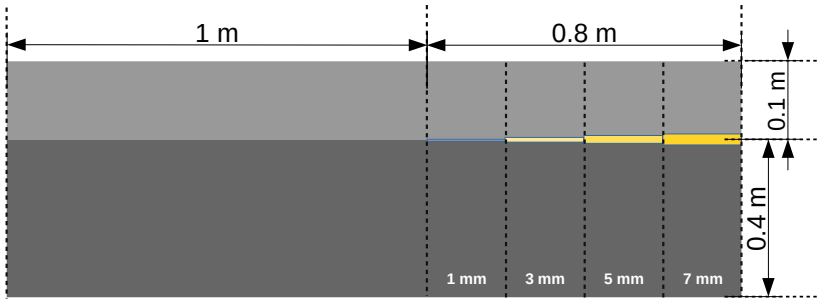

Figure 13: Pavement structure model used to generate a B-scan with defective zone containing debondings of respectively $1\,\mathrm{mm}$, $3\,\mathrm{mm}$, $5\,\mathrm{mm}$ and $7\,\mathrm{mm}$ thicknesses. Antennas are positioned respectively as shown in Figure 3

and SF-GPR configurations of the pavement model from Figure 13. For both SF-GPR and GC-GPR configurations, zero non-detection (*i.e.*, FN) were observed. However, some false alarms were seen to occur in both cases leading to the DSC scores of 0.98 and 0.99 for respectively GC-GPR and SF-GPR configurations.

Since the SF-GPR operates at a higher frequency, the time resolution of its data is higher. This provides a better feature separation and therefore has a better performance than the GC-GPR data.

In the final section, we implement One-class SVM debonding detection method on experimental data collected at the IFSTTAR's APT site using both air-launched and ground-coupled radar configurations.

5. Experimental validation of OCSVM

In this section, the proposed method is tested on the experimental data presented in Section 5. Here, the OCSVM model optimization and the debonding detection process is the same as done for GprMax pavement model in Section 4. Two pavement sections are probed with the GPR. The first is the known pavement section with no debondings consisting of $N = 20$ A-scans and is used for the 'learning' step (as done in Section 4). The second section is then probed whose subsurface condition is unknown. This unknown B-scan is divided by the operator into two groups namely, transition zone and testing zone. The transition zone is the region where the presence/absence of debond-

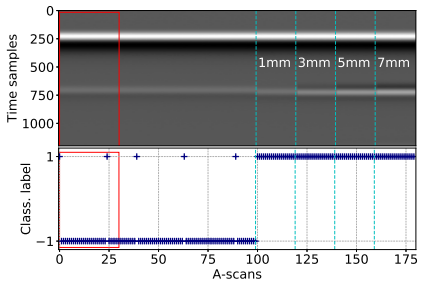

(a) Ground coupled GPR configuration

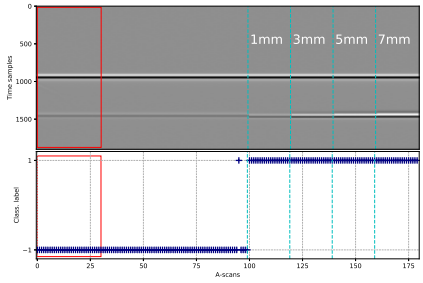

(b) Air-launched GPR configuration

Figure 14: One-class SVM debonding detection on noisy GprMax data (SNR = 30 dB, $N_{learn} = 30$) with various debonding thicknesses th_{deb} = 1 mm, 3 mm, 5 mm and 7 mm. The solid box indicates the learning data; vertical dashed lines indicate various thickness zones

ing is ambiguous and this zone is excluded from the performance evaluation of the detection method.

Loading stages	*SFR*	*GSSI*
10K	0.96	0.93
50K	0.97	0.9
100K	0.96	0.96

Table 1: Debonding detection DSC score for Tack-free defects at various loading stages for SFR and GSSI-GPR data

Table 1 presents DSC score for Tack-free defects each at various loading stages. Figures 15, 16 and 17 present the detection results for Tack-free defects at 10K, 50K and 100K cycles loading stages. The first $N = 20$ A-scans is the known region used for the learning step. In each figure, the region between the dashed lines is the transition zone. The remainder is the testing B-scan data.
In case of experimental data, the thickness of Tack-free defects was observed to be between 2 mm to 3 mm (see Section 2.1). The OCSVM method provided similar results for GC-GPR and SF-GPR data at 10K and 100K loading. However the performance in case of GC-GPR data at 50K loading was reduced due to aberrant A-scans present in

the learning data.

From Figures 15, 16 and 17 and Table 1, it can be observed that OCSVM is capable of detecting debondings with high efficiency and very few false alarms. These false alarms could be attributed to the data-points present very close to the OCSVM hyper-sphere boundary. The zone in the blue box indicates the learning data and t_{zone} denotes the transition zone. In general, it was observed that the performance of the OCSVM

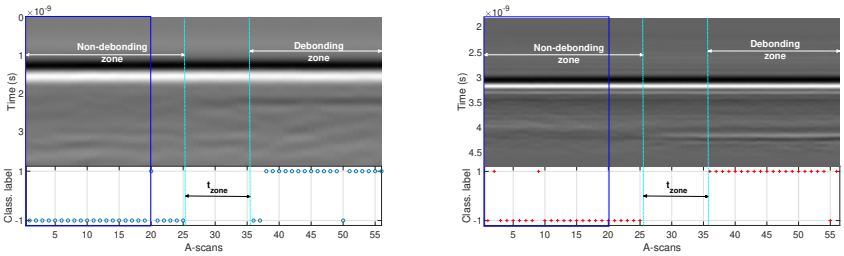

(a) Tack-free: GSSI data (b) Tack-free: SFR data

Figure 15: Debonding detection at 10K loading for for Tack-free based defects

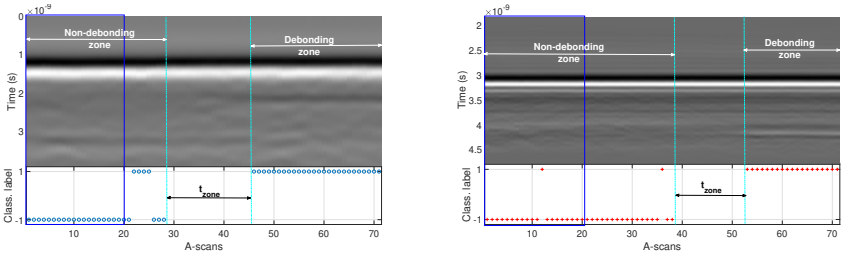

(a) Tack-free: GSSI data (b) Tack-free: SFR data

Figure 16: Debonding detection at 50K loading for for Tack-free based defects

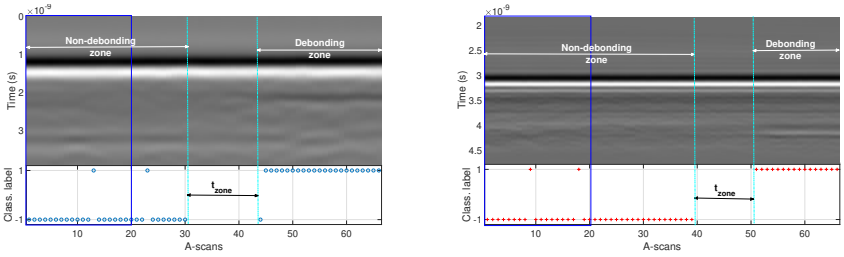

(a) Tack-free: GSSI data (b) Tack-free: SFR data

Figure 17: Debonding detection at 100K loading for for Tack-free based defects

method was always slightly better for SF-GPR that the GC-GPR data. This observation was held true for both synthetic GprMax as well as experimental data. The SF-GPR

operates at a higher frequency ($f_{c,SFR} = 4.2\,\mathrm{GHz}$) compared to the GC-GPR operating at $f_{c,GSSI} = 2.6\,\mathrm{GHz}$. The higher temporal resolution allows the SF-GPR to provide better distinction between the interface echoes and therefore, better separated features of the two classes.

However, the OCSVM method has a few limitations. In this paper, a known non-debonding dataset is used to train the OCSVM model. The presence of debonding data (outliers) in this learning dataset could skew the classification model leading to false detection (False Negative and/or False Positive). OCSVM is also limited by the number of classes for classification (inliers or outliers); this method cannot be used for multi-class classification.

6. Comparison between One-class and Two-class SVMs

In this section, we compare the performance of One-class and Two-class SVM (from (Todkar et al., 2019)). Contrary to OCSVM, the Two-class SVM requires data from both classes during the learning stage. The best separation in this case is intuitively achieved with the hyper-plane which provides the maximum distance from the nearest data-points of the debonding and non-debonding classes.

In case of Two-class SVM, the initial data set (*i.e.*, 10K loading) for each defect was used in the learning stage to generate a classification model. This approach is suitable for a long-term detection while the initial conditions is available. OCSVM in this paper is more of an immediate/short-term detection approach because it does not require an initial data set. Detection is carried out on each loading stage independent of the previous data. Since (Todkar et al., 2019) performs detection on SF-GPR data only, we compare the same with OCSVM results. For the sake of relevance, we cover the two extreme cases and the results for strong (Geotextile) defects are presented in addition to Tack-free defect data.

The Two-class SVM detection (as presented in (Todkar et al., 2019)) for SF-GPR data uses approximately 50% of its data as learning data. OCSVM, on the contrary, uses a smaller learning data (first 20 A-scans, which is about 20% - 25%) to provide very similar results. Table 2 and Table 3 compare the DSC scores of One-class and Two-class SVMs for Tack-free and Geotextile defects respectively. It can be noted that in case of Tack-free defects, both One and Two-class SVMs provide similar performance.

Both One and Two-class SVMs demonstrate good performance. However, OCSVM

Loading stage	Two-class SVM	One-class SVM
10K	$1.0^{\dagger}$	0.96
50K	0.96	0.97
100K	0.95	0.96

Table 2: Comparison of DSC score for Tack-free defects at various loading stages obtained using Two-class and One-class SVMs (Two-class detection results taken from (Todkar et al., 2019))

Loading stage	Two-class SVM	One-class SVM
10K	1.0[†]	0.96
50K	1.0	1.0
100K	1.0	0.95

Table 3: Comparison of DSC score for Geotextile defects at various loading stages obtained using Two-class and One-class SVMs (Two-class detection results taken from (Todkar et al., 2019))

relies on the non-debonding data which is readily available contrary to the two-class and a smaller learning dataset size. In addition, since OCSVM does not require initial data, it is well-suited to be used in field detection for short-term practical experiments.

7. Conclusion

In this article, we proposed to implement OCSVM for detecting thin debondings from both air-coupled and ground-coupled GPR data. The proposed approach was first tested with simulated pavement models from GprMax. To study its capability to adapt to various data configurations, OCSVM Sensitivity Analysis was conducted.
With the help of OCSVM, we were able to detect debondings with $DSC > 0.75$ (for GC-GPR) and $DSC > 0.98$ (for SF-GPR) at an SNR= 20 dB or greater. At a small learning data size of $N_{learn} = 5$, GC-GPR showed a $DSC > 0.8$ in contrast to the SF-GPR with $DSC > 0.85$. The performance reached close to $DSC \approx 1$ as the learning data size was gradually increased. In addition, OCSVM was able to detect thin debondings within a B-scan varying from $1\,\mathrm{mm}$ to $7\,\mathrm{mm}$ from both GC and SF-GPR with very few false detection. Overall, for simulated data, the OCSVM method performed better with SF-GPR data sets than its counterpart GC-GPR data sets.
The OCSVM was then validated on experimental data collected with two GPR configurations over embedded Tack-free defects. Over three loading stages (10K, 50K and 100K), due to its increased temporal resolution and better separated signals in the time domain, OCSVM provided better results for SF-GPR compared to the GC-GPR data sets.
Finally, a short comparison to the previous works showed that the OCSVM method provided similar results as its Two-class counterpart. It was observed that OCSVM is suited for short-term debonding detection experiments.
In perspective, we aim to extend the performance assessment of the proposed detection method to the entire data set collected over the tested pavement structure during its entire lifetime, *i.e.*, up to 800K loading.

[†](Todkar et al., 2019) used 10K data set as learning and the remaining loading sets as test; contrast to the OCSVM in this paper that uses the first 20 A-scans of each loading for learning

Acknowledgment

The French National Research Agency (ANR) is gratefully acknowledged for supporting the ANR-ACIMP project (Project code: ANR-18-CE22-0020).

Appendix A. Computation of SNR from experimental data

In this appendix, we present, in brief, the estimation of SNR from experimental SF-GPR data.
Revisiting Equation 9 for SNR computation, we have:

$$SNR = 20 * \log\left\{\frac{M}{\sigma_N}\right\} \tag{A.1}$$

Now, in order to compute the SNR from experimental data, two values, namely M and σ_N are required. The value for M is obtained from the known learning data (non-debonding zone) using the automatic time-gating window (Section 3.2). The standard deviation of the noise (σ_N) is computed from the late arrival signals of the subsequent layers as shown in Figure A.18.
To summarize, Table A.4 provides the SNR levels for all loading stages obtained for

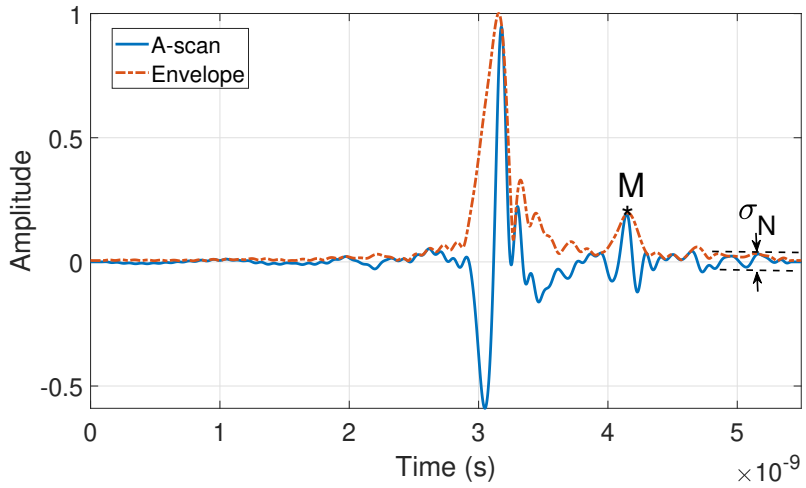

Figure A.18: Illustration of the SNR computation for GPR data from Equation 9 over the Tack-free defect at 10K loading

Tack-free defects.

References

Benedetto, A., Tosti, F., Ciampoli, L.B., DAmico, F., 2017. An overview of ground-penetrating radar signal processing techniques for road inspections. Signal Processing 132, 201 – 209. doi:10.1016/j.sigpro.2016.05.016.

Loading stage	SNR (dB)
10K	22.8
50K	21.9
100K	22.3

Table A.4: Estimated average SNR (in dB) of the debonded interface echo over Tack-free area at all loading stages

Büyüköztürk, O., Yu, T.Y., 2006. Understanding and assessment of debonding failures in frp-concrete systems, in: Seventh International Congress on Advances in Civil Engineering, Citeseer. pp. 11–13.

Chang, C.C., Lin, C.J., 2011. LIBSVM: A library for support vector machines. ACM Transactions on Intelligent Systems and Technology 2, 27:1–27:27. Software available at http://www.csie.ntu.edu.tw/~cjlin/libsvm.

Chen, Y., Zhou, X.S., Huang, T.S., 2001. One-class svm for learning in image retrieval, in: Proceedings 2001 International Conference on Image Processing, pp. 34–37. doi:10.1109/ICIP.2001.958946.

Dérobert, X., Baltazart, V., Simonin, J.M., Norgeot, C., Doué, S., Durand, O., Todkar, S.S., 2020. Radar database collected over artificial debonding pavement structures during apt at the ifsttar's fatigue carrousel, in: Chabot, A., Hornych, P., Harvey, J., Loria-Salazar, L.G. (Eds.), Accelerated Pavement Testing to Transport Infrastructure Innovation, Springer International Publishing, Cham. pp. 632–639.

Diakité, C., Fortino, N., Dauvignac, J.Y., 2015. Antenne ETSA "Exponential Tapered Slot Antenna" miniature pour radar à pénétration de surface, in: 19èmes Journées Nationales Microondes (JNM 2015), Bordeaux, France. pp. Session Antennes large bande et multibandes C3L–D, papier 9337.

Dong, Z., Ye, S., Gao, Y., Fang, G., Zhang, X., Xue, Z., Zhang, T., 2016. Rapid detection methods for asphalt pavement thicknesses and defects by a vehicle-mounted ground penetrating radar (gpr) system. Sensors 16. doi:10.3390/s16122067.

Dreiseitl, S., Osl, M., Scheibböck, C., Binder, M., 2010. Outlier detection with one-class svms: An application to melanoma prognosis. AMIA: Annual Symposium proceedings. AMIA Symposium 2010, 172–176.

Dérobert, X., Baltazart, V., 2012. Report on step-frequency radar data collection on the fatigue carousel. Personal communication (2012) .

Dérobert, X., Baltazart, V., Simonin, J.M., Norgeot, C., Durand, O., Todkar, S., 2020. Radar database over large debonded areas into pavement structures. doi:10.25578/N0RXSQ.

Ebrahim, S.M., Medhat, N., Mansour, K.K., Gaber, A., 2018. Examination of soil effect upon gpr detectability of landmine with different orientations. NRIAG Journal of Astronomy and Geophysics 7, 90 – 98. doi:10.1016/j.nrjag.2017.12.004.

Eude, T., Chang, C., 2018. One-class svm for biometric authentication by keystroke dynamics for remote evaluation. Computational Intelligence 34, 145–160. doi:10.1111/coin.12122.

Giannopoulos, A., 2005. Modelling ground penetrating radar by gprmax. Construction and building materials 19, 755–762.

Gu, H., Zhao, G., Qiu, J., 2010. One-class support vector machine with relative comparisons. Tsinghua Science and Technology 15, 190–197. doi:10.1016/S1007-0214(10)70049-3.

Hajj, E., Loria, L., Sebaaly, P., 2010. Performance evaluation of asphalt pavement preservation activities. Transportation Research Record 2150, 36 – 46.

Huang, T.S., 2001. One-class svm for learning in image retrieval, in: Proceedings 2001 International Conference on Image Processing (Cat. No.01CH37205), pp. 34–37 vol.1. doi:10.1109/ICIP.2001.958946.

Kaplanvural, I., Peksen, E., Özkap, K., 2018. Volumetric water content estimation of c-30 concrete using gpr. Construction and Building Materials 166, 141 – 146. doi:10.1016/j.conbuildmat.2018.01.132.

Kulkarni, A., Chong, D., Batarseh, F.A., 2020. 5 - foundations of data imbalance and solutions for a data democracy, in: Batarseh, F.A., Yang, R. (Eds.), Data Democracy. Academic Press, pp. 83 – 106. doi:https://doi.org/10.1016/B978-0-12-818366-3.00005-8.

Kumar, G., Bhatia, P.K., 2014. A detailed review of feature extraction in image processing systems, in: 2014 Fourth International Conference on Advanced Computing Communication Technologies, pp. 5–12. doi:10.1109/ACCT.2014.74.

Li, K.L., Huang, H.K., Tian, S.F., Xu, W., 2003. Improving one-class svm for anomaly detection, in: Proceedings of the 2003 International Conference on Machine Learning and Cybernetics, IEEE Computer Society, Los Alamitos, CA, USA. pp. 3077,3078,3079,3080,3081. doi:10.1109/ICMLC.2003.1260106.

Liu, H., Motoda, H., 1998. Feature Selection Aspects. Springer US, Boston, MA. pp. 43–72. doi:10.1007/978-1-4615-5689-3_3.

Mei, S., Zhu, H., 2015. A novel one-class svm based negative data sampling method for reconstructing proteome-wide htlv-human protein interaction networks, in: Scientific reports, pp. 1–13. doi:10.1038/srep08034.

Nesbitt, I., Simon, F.X., Paulin, T., 2019. readgssi: an open-source tool to read and plot GSSI ground-penetrating radar data. doi:10.5281/zenodo.3352438.

Pedregosa, F., Varoquaux, G., Gramfort, A., Michel, V., Thirion, B., Grisel, O., Blondel, M., Prettenhofer, P., Weiss, R., Dubourg, V., Vanderplas, J., Passos, A., Cournapeau, D., Brucher, M., Perrot, M., Duchesnay, E., 2011. Scikit-learn: Machine learning in Python. Journal of Machine Learning Research 12, 2825–2830.

Peeters, G., 2004. A large set of audio features for sound description (similarity and classification) in the CUIDADO project. Technical Report. Icram.

Pinel, N., Le Bastard, C., Liu, L., Bourlier, C., Wang, Y., 2009. Rough thin pavement thickness estimation by GPR, in: International Geoscience and Remote Sensing Symposium, Le Cap (Cape Town), South Africa. p. 1255. 4 pages.

Salem, M.B., Stolfo, S.J., 2012. A comparison of one-class bag-of-words user behavior modeling techniques for masquerade detection. Sec. and Commun. Netw. 5, 863–872. doi:10.1002/sec.311.

Samadzadegan, F., Hasani, H., Partovi, T., 2010. Sensitivity analysis of support vector machine in classification of hyperspectral imagery, in: Proceedings of the Canadian Geomatics Conference, Calgary, Canada, pp. –.

Schölkopf, B., Platt, J.C., Shawe-Taylor, J.C., Smola, A.J., Williamson, R.C., 2001. Estimating the support of a high-dimensional distribution. Neural Comput. 13, 1443–1471. doi:10.1162/089976601750264965.

Senf, A., Chen, X.w., Zhang, A., 2006. Comparison of one-class svm and two-class svm for fold recognition, in: King, I., Wang, J., Chan, L.W., Wang, D. (Eds.), Neural Information Processing, Springer Berlin Heidelberg, Berlin, Heidelberg. pp. 140–149.

Siegwart, R., Nourbakhsh, I.R., Scaramuzza, D., 2011. Introduction to Autonomous Mobile Robots: Perception. MITP. pp. 101–263.

Simonin, J.M., Baltazart, V., Le Bastard, C., Dérobert, X., 2016. Progress in monitoring the debonding within pavement structures during accelerated pavement testing on the fatigue carousel, in: 8th RILEM International Conference on Mechanisms of Cracking and Debonding in Pavements, Springer Netherlands, Dordrecht. pp. 749–755.

Simonin, J.M., Fauchard, C., Hornych, P., Guilbert, V., Kerzrého, J.P., Trichet, S., 2012. Detecting unbounded interface with non destructive techniques, in: Scarpas, A., Kringos, N., Al-Qadi, I., A., L. (Eds.), 7th RILEM International Conference on Cracking in Pavements, Springer Netherlands, Dordrecht. pp. 179–190.

Tax, D.M., Duin, R.P., 2004. Support vector data description. Machine Learning 54, 45–66. doi:10.1023/B:MACH.0000008084.60811.49.

Tbarki, K., Said, S.B., Ksantini, R., Lachiri, Z., 2017a. Landmine detection improvement using one-class svm for unbalanced data, in: 2017 International Conference on Advanced Technologies for Signal and Image Processing (ATSIP), pp. 1–6. doi:10.1109/ATSIP.2017.8075597.

Tbarki, K., Said, S.B., Ksantini, R., Lachiri, Z., 2017b. One-class svm for landmine detection and discrimination. 2017 International Conference on Control, Automation and Diagnosis (ICCAD) , 309–313.

Tbarki, K., Said, S.B., Ksantini, R., Lachiri, Z., 2018. Covariance-guided landmine detection and discrimination using ground-penetrating radar data. International Journal of Remote Sensing 39, 289–314. doi:10.1080/01431161.2017.1382746.

Tellez, O.L.L., Scheers, B., 2017. Ground-penetrating radar for close-in mine detection. Mine Action: The Research Experience of the Royal Military Academy of Belgium , 51.

Thomas, A., Feuillard, V., Gramfort, A., 2015. Calibration of one-class svm for mv set estimation, in: 2015 IEEE International Conference on Data Science and Advanced Analytics (DSAA), IEEE. pp. 1–9.

Todkar, S.S., 2019. Monitoring subsurface conditions of pavement structures using Ultra-wideband radar technology. Ph.D. thesis. University of Nantes, France.

Todkar, S.S., Bastard, C.L., Baltazart, V., Ihamouten, A., Dérobert, X., 2019. Performance assessment of svm-based classification techniques for the detection of artificial debondings within pavement structures from stepped-frequency a-scan radar data. NDT & E International 107, 102128. doi:https://doi.org/10.1016/j.ndteint.2019.102128.

Todkar, S.S., Bastard, C.L., Ihamouten, A., Baltazart, V., Dérobert, X., 2018. Comparative study of classification algorithms to detect interlayer debondings within pavement structures from step-frequency radar data, in: 2018 38th Annual IEEE Geoscience and Remote sensing society(IGARSS), pp. 1–6. doi:10.1109/IWAGPR.2017.7996056.

Todkar, S.S., Bastard, C.L., Ihamouten, A., Baltazart, V., Dérobert, X., Fauchard, C., Guilbert, D., Bosc, F., 2017. Detection of debondings with ground penetrating radar using a machine learning method, in: 2017 9th International Workshop on Advanced Ground Penetrating Radar (IWAGPR), pp. 1–6. doi:10.1109/IWAGPR.2017.7996056.

Wai-Lok Lai, W., Dérobert, X., Annan, P., 2018. A review of ground penetrating radar application in civil engineering: A 30-year journey from locating and testing to imaging and diagnosis. NDT & E International 96, 58–78. doi:https://doi.org/10.1016/j.ndteint.2017.04.002.

Warren, C., Giannopoulos, A., Giannakis, I., 2015. An advanced gpr modelling framework: The next generation of gprmax, in: 2015 8th International Workshop on Advanced Ground Penetrating Radar (IWAGPR), pp. 1–4. doi:10.1109/IWAGPR.2015.7292621.

Wright, D., Baltazart, V., Elsworth, N., Hamrouche, R., Karup, J., Lurdes Antunes, M., McRobbie, S., Merecos, V., Saarenketo, T., 2014. D4.3 monitoring structural and surface conditions (technical report) Eur. Comm. DG Res., Tech. Rep FP7-285119.

692 Zaki, A., Megat Johari, M.A., Wan Hussin, W.M.A., Jusman, Y., 2018. Experimental
693 assessment of rebar corrosion in concrete slab using ground penetrating radar (gpr).
694 International Journal of Corrosion , 1–10doi:10.1155/2018/5389829.